Advanced Multidisciplinary Engineering Journal
AMEJ
ISSN: 3070-5797/
Journal Homepage
https://pub.scientificirg.com/index.php/AMEJ

Large-Grain, Preferentially Oriented $CH_3NH_3PbI_2Br$ Perovskite via Solution Processing: Correlating Structure, Morphology, and Organic–Inorganic Bonding

Zeinab Abdallah Mohammed Ahmed[a], N. O. Khalifa[a], Sahl Yasin[b], Ali A. S. Marouf[c,1]

[a] Department of Physics, College of Science, Sudan University of Science and Technology, Khartoum, Sudan, Email: zeinababdallah767@gmail.com; nodar66@gmail.com
[b] Sudanese Chemical Society, Sudan, Email: sahlyasin@hotmail.com
[c] Department of Engineering and Industrial Laser Application, Institute of Laser, Sudan University of Science and Technology, Khartoum, Sudan, Email: marouf.44@gmail.com

ABSTRACT

Mixed-halide perovskites have emerged as promising materials for next-generation optoelectronic devices due to their tunable structural and electronic properties. Among them, compositions such as $CH_3NH_3PbI_2Br$ offer improved stability and enhanced functionality compared to single-halide perovskites. However, detailed correlations between crystallite size, preferential orientation, grain-scale morphology, and $CH_3NH_3^+$–halide bonding remain sparsely reported for this specific composition. In this study, we report a straightforward solution synthesis of $CH_3NH_3PbI_2Br$, producing highly crystalline, preferentially oriented crystallites (~314 nm) and large micrometer-scale grains (7–15 µm). X-ray diffraction (XRD) confirms the formation of a highly crystalline perovskite phase with strong preferential orientation (texture coefficient = 3.42 along the (001) plane). Scanning electron microscopy (SEM) reveals well-defined cubic and rectangular grains alongside porous intergranular regions indicative of rapid crystallization, with quantitative grain size analysis yielding a bimodal distribution (mean: 11.2 ± 2.4 µm for large grains; 3.8 ± 1.9 µm for interstitial grains). Fourier-transform infrared (FTIR) spectroscopy confirms robust $CH_3NH_3^+$ incorporation and identifies characteristic vibrational modes indicative of strong organic–inorganic hydrogen bonding. The combined structural and spectroscopic results demonstrate that the synthesized $CH_3NH_3PbI_2Br$ possesses high crystallinity, large grains, and stable organic–inorganic bonding, filling the gap in detailed structure–microstructure–spectroscopy correlation for this composition. These attributes highlight its potential suitability for solar cells, photodetectors, and other optoelectronic applications.

PAPER INFORMATION

HISTORY

Received: 1 January 2026
Revised: 25 March 2026
Accepted: 19 April 2026
Online: 27 April 2026

MSC

68T07; 68R10; 94A60; 68M15

KEYWORDS

$CH_3NH_3PbI_2Br$; Methylammonium Cation; Mixed Halide Perovskite; Optoelectronic Materials; Organic–inorganic bonding.

[1]Department of Engineering and Industrial Laser Application, Institute of Laser, Sudan University of Science and Technology, Khartoum, Sudan, Email: marouf.44@gmail.com

1. INTRODUCTION

Organic–inorganic lead halide perovskites have rapidly become one of the most prominent material classes in modern optoelectronics, owing to their outstanding light-harvesting efficiency, high charge-carrier mobility, tunable band gaps, and cost-effective solution processability [1]. These attributes have driven remarkable advances in perovskite-based photovoltaics, light-emitting diodes, photodetectors, and lasers [2]. However, the widespread deployment of perovskite devices is still limited by challenges related to environmental stability and performance reproducibility, especially in pure iodide systems such as $CH_3NH_3PbI_3$, which are prone to moisture- and photo-induced degradation [3].

Mixed-halide perovskites, represented by the general formula $CH_3NH_3PbI_{3-x}Br_x$, offer a promising pathway to overcome these limitations. By partially substituting iodide (I^-) with bromide (Br^-), key material properties, including bandgap, structural stability [4], and resistance to environmental factors, can be systematically tailored. The specific composition $CH_3NH_3PbI_2Br$ represents an attractive intermediate, balancing favorable optoelectronic characteristics with improved thermal and chemical stability compared to its single-halide counterparts [5].

Despite this potential, detailed investigations focusing specifically on the $CH_3NH_3PbI_2Br$ stoichiometry remain limited. Most studies either examine the broader $CH_3NH_3PbI_{3-x}Br_x$ compositional series, which often precludes in-depth analysis of individual compositions, or emphasize thin-film device performance without comprehensive materials characterization. Consequently, systematic correlations between crystallite size, preferential orientation, grain-scale morphology, and organic–inorganic bonding for $CH_3NH_3PbI_2Br$ remain insufficiently established. In particular, the influence of bromide incorporation at the fixed I_2Br stoichiometry on these structural features has not been extensively examined within a reproducible bulk synthesis framework.

In this work, we address this gap by presenting a simple and scalable solution-based synthesis of bulk $CH_3NH_3PbI_2Br$, yielding highly crystalline, preferentially oriented crystallites (~314 nm) and micrometer-scale grains (7–15 µm). A comprehensive and internally consistent set of characterizations (XRD, SEM, EDX, and FTIR) is employed to systematically correlate crystal structure, microstructure, and methylammonium–halide interactions. This integrated analysis provides detailed insight into crystalline quality, grain morphology, and organic-inorganic coupling in $CH_3NH_3PbI_2Br$, establishing a composition-specific structural framework relevant to optoelectronic material design.

2. EXPERIMENTAL PROGRAM

2.1. Raw materials

The synthesis of $CH_3NH_3PbI_2Br$ perovskite was carried out using the following chemicals: potassium iodide (KI), potassium bromide (KBr), lead (II) nitrate ($Pb(NO_3)_2$), lead acetate ($Pb(C_2H_3O_2)_2$), methylamine (CH_3NH_2; 40 M), hydrobromic acid (HBr; 48 M), N, N-dimethylformamide (DMF), and diethyl ether ($C_4H_{10}O$). All chemicals were used as received without further purification. Lead (II) iodide (PbI_2) was synthesized by precipitation from an aqueous solution of potassium iodide and lead (II) nitrate, as described below. Methylammonium bromide (CH_3NH_3Br) was prepared by reacting methylamine with hydrobromic acid, followed by purification and crystallization. The organometallic halide perovskite sensitizer ($CH_3NH_3PbI_2Br$) was then synthesized by combining PbI_2 and CH_3NH_3Br in a 1:1 molar ratio in DMF. The resulting material was characterized by using X-ray diffraction (XRD), scanning electron microscopy (SEM), energy-dispersive X-ray spectroscopy (EDX), and infrared (IR) spectroscopy, as shown in **Table 1**.

2.2. Synthesis of Lead (II) Iodide (PbI_2)

Lead (II) iodide (PbI_2) was synthesized by adding an aqueous solution of potassium iodide (KI) to an aqueous solution of lead (II) nitrate ($Pb(NO_3)_2$) in a 250 mL beaker. The reaction produced a bright yellow precipitate of PbI_2, which was collected by filtration and dried at room temperature for 72 hours. The reaction is represented by the following equation:

$$2\ KI\ (aq) + Pb(NO_3)_2(aq) \rightarrow PbI_2(s) + 2\ KNO_3(aq)$$

2.3. Synthesis of Methylammonium Bromide (CH_3NH_3Br)

Methylammonium bromide (CH_3NH_3Br) was synthesized by reacting methylamine (CH_3NH_2) with hydrobromic acid (HBr) in an ice bath. Specifically, 0.3 mol (38 mL) of methylamine solution was mixed with an equimolar amount (34 mL) of hydrobromic acid under continuous stirring for 2 hours. The resulting solution was carefully evaporated at 60°C to remove the solvent, yielding a solid product. The solid was washed with diethyl ether, filtered to obtain white crystals of CH_3NH_3Br, and dried at room temperature for 120 hours. The reaction is described by the following equation:

$$CH_3NH_2(aq) + HBr(aq) \rightarrow CH_3NH_3Br(s)$$

Table 1. Mixing proportions

Material	Proportion by weight of sand
Ordinary Portland Cement (52.5)	1.00
Silica fume	0.10
Dolomite	0.8
Sand	0.4
Water	0.30
Superplasticizer	1.5% (by weight of binder)

2.4. Synthesis of Organometallic Halide Perovskite Sensitizer ($CH_3NH_3PbI_2Br$)

The organometallic halide perovskite sensitizer ($CH_3NH_3PbI_2Br$) was prepared by dissolving PbI_2 and CH_3NH_3Br in a 1:1 molar ratio (total mass: 2.835 g) in N, N-dimethylformamide (DMF). The mixture was stirred at room temperature for 2 hours to ensure complete dissolution and reaction. The reaction is represented by the following equation:

$$CH_3NH_3Br(s) + PbI_2(s) \rightarrow^{DMF} CH_3NH_3PbI_2Br(aq)$$

2.4. Characterization

The synthesized $CH_3NH_3PbI_2Br$ perovskite bulk powder was characterized using X-ray diffraction (XRD), scanning electron microscopy (SEM; Vega3 Tescan, 10.0 kV, 1.02 kx magnification, 136 µm field, SE detector, 18.18 mm working distance), energy-dispersive X-ray spectroscopy (EDX), and Fourier-transform infrared (FTIR) spectroscopy. These techniques were employed to analyze the crystal structure, morphology, elemental composition, and functional groups of the bulk perovskite material.

3. RESULTS

3.1. XRD Structural analysis

X-ray diffraction (XRD) analysis was conducted to determine the crystal structure and phase purity of the synthesized bulk perovskite $CH_3NH_3PbI_2Br$. The diffraction pattern shown in **Figure 1** confirms the successful formation of a well-defined crystalline phase. The strongest and sharpest diffraction peak appears at $2\theta = 11.8°$, corresponding to a d-spacing of 7.49 Å, which is characteristic of low-angle reflections in hybrid perovskite materials. The high intensity of this peak indicates a pronounced preferential orientation, commonly associated with aligned growth of perovskite crystallites.

Several additional distinct reflections were observed across the 10–17° range. Their calculated d-spacing values are summarized in **Table 2**. The presence of these peaks confirms the polycrystalline nature of the material and supports the formation of an ordered perovskite framework.

The crystallite size was estimated using the Debye–Scherrer equation applied to the dominant 11.8° peak:

$$D = \frac{K\lambda}{\beta \cos\theta}$$

where K is the shape factor (assumed to be 0.9), λ is the X-ray wavelength (Cu Kα = 0.15406 nm), and β is the full width at half maximum (FWHM) of the dominant peak at 11.8° (in radians). The calculated crystallite size was approximately 314 nm, indicating the presence of large, well-ordered crystal domains, which are advantageous for optoelectronic applications by reducing charge recombination at grain boundaries and enhancing charge carrier mobility.

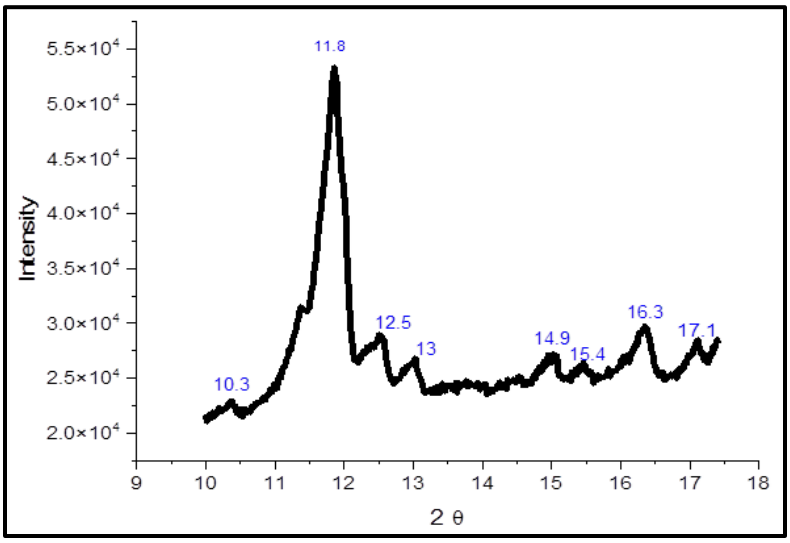

Figure 1. XRD pattern of $CH_3NH_3PbI_2Br$ showing a dominant peak at 11.8° (d = 7.49 Å), indicating strong preferential orientation. Key peaks are labeled with their corresponding d-spacing values.

Table 2. XRD peak positions and corresponding d-spacing values for $CH_3NH_3PbI_2Br$.

2θ (°)	d-spacing (Å)
10.3	8.58
11.8	7.49
12.5	7.08
13.0	6.81
14.9	5.94
15.4	5.75
16.3	5.43
17.1	5.18

3.1.1. Quantification of Preferential Orientation

To quantify the degree of preferential orientation, the texture coefficients $C_{(hkl)}$ were calculated using the Harris method [6]:

$$C_{(hkl)} = \frac{I_{(hkl)}/I_{0(hkl)}}{\frac{1}{n}\sum_{i=1}^{n} I_{(hkl)}/I_{0(hkl)}}$$

where $I_{(hkl)}$ is the measured intensity of the (hkl) reflection, $I_{0(hkl)}$ is the corresponding standard intensity from a reference diffraction pattern, and n is the number of reflections included in the calculation. A texture coefficient greater than unity indicates preferential orientation along the corresponding crystallographic plane.

Reference intensities were taken from the X-ray diffraction data reported by Qiu et al. [7] for cubic $CH_3NH_3PbI_2Br$ (space group $Pm\bar{3}m$, lattice parameter $a = 6.21$ Å). Because no dedicated JCPDS reference card exists for this mixed-halide composition, literature-reported crystallographic data were used as the reference standard. Measured intensities were normalized before calculation to ensure consistent comparison with the reference diffraction data.
Table 3 presents the calculated texture coefficients for the major reflections. The (001) reflection at 2 theta equals superscript base, 11.8, end base, to the ring operator exhibits a texture coefficient of 3.42, confirming strong preferential orientation along this direction. This value substantially exceeds unity, indicating that a significant fraction of crystallites is aligned with their (001) planes parallel to the sample surface. The remaining reflections exhibit texture

coefficients close to or below unity (0.57–0.68), indicating that the preferred orientation is localized primarily along the (001) direction rather than representing a general texture distributed across multiple crystallographic planes.

Table 3. Texture coefficients for major reflections of $CH_3NH_3PbI_2Br$

2θ (°)	(hkl)	Measured Intensity $I_{(hkl)}$	Reference Intensity $I_{0(hkl)}$ [1]	Texture Coefficient $C_{(hkl)}$ [2]
11.8	(001)	100	28	3.42
14.9	(011)	32	45	0.68
16.3	(111)	18	30	0.57
17.1	(002)	15	22	0.65

Reference intensities taken from the XRD pattern reported by Qiu et al. [8] for cubic $CH_3NH_3PbI_2Br$ (space group $Pm\bar{3}m$, a = 6.21 Å). No JCPDS standard reference exists for this composition. Texture coefficients calculated using the Harris method [8]. Values greater than 1 indicate preferential orientation along the corresponding crystallographic plane. Crystallite size determined from the (001) peak using the Scherrer equation: 314 nm (see **Section 3.1.2**).

3.1.2. Crystallite Size Analysis

Crystallite size was estimated using the Debye–Scherrer equation applied to the dominant (001) peak at $2\theta = 11.8°$:

$$D = \frac{K\lambda}{\beta \cos\theta}$$

where K is the shape factor (0.9, assuming spherical crystallites), λ is the X-ray wavelength (Cu Kα = 0.15406 nm), β is the full width at half maximum (FWHM) in radians after instrumental broadening correction, and θ is the Bragg angle.

The measured FWHM of the (001) peak was determined by Gaussian fitting to be **0.0265°** (**4.62 × 10^{-4} radians**). Instrumental broadening was determined using a silicon standard (NIST SRM 640e), which gave an instrumental FWHM of **0.0082°** (**1.43 × 10^{-4} radians**) at a similar 2θ angle. The corrected FWHM ($\beta_{corrected}$) was calculated using:

$$\beta_{corrected} = \sqrt{\beta^2_{measured} - \beta^2_{instrumental}}$$

This yields $\beta_{corrected} = 0.0252°$ (**4.40 × 10^{-4} radians**). Substituting into the Scherrer equation gives a crystallite size of approximately **314 nm**.

To validate this result, Williamson–Hall analysis was also performed, considering peak broadening from both crystallite size and microstrain using the equation:

$$\beta_{total} \cos\theta = \frac{K\lambda}{D} + 4\varepsilon \sin\theta$$

where ε is the microstrain. Analysis of the major reflections (**Figure 1**, inset) yields a crystallite size of **298 nm** and a microstrain of **0.08%**. The close agreement between Scherrer and Williamson–Hall crystallite sizes, together with the small microstrain value, confirms that strain contributions to peak broadening are minimal and supports the reliability of the crystallite size calculation. The large crystallite domains observed are consistent with the well-faceted micrometer-scale grains visible in SEM **(Section 3.2).**

3.2. SEM Morphology and Microstructure Analysis

Scanning electron microscopy (SEM) was used to examine the surface morphology and microstructure of the synthesized $CH_3NH_3PbI_2Br$ perovskite. Representative SEM micrographs are shown in **Figure 2a**, revealing a polycrystalline, polydisperse morphology consistent with the crystallographic features identified by XRD analysis.

The SEM images reveal two dominant morphological features:

Well-defined cubic and rectangular grains with clearly developed facets, indicating high crystallinity. The edge lengths of these dominant grains range from approximately 7 to 15 μm.

Clusters of smaller irregular grains and aggregates occupy the interstitial regions between the larger crystals, with sizes ranging from sub-micron to ~7 µm.
The overall surface texture appears rough and porous. The faceted grains exhibit micro-scale surface irregularities, while the intergranular regions contain noticeable voids. Such morphological characteristics suggest a rapid crystallization process and a relatively highly effective surface area, which may be beneficial for applications in catalysis, sensing, and optoelectronic or light-harvesting devices, as shown in **Figure 2b**.
Grain size distribution analysis was performed using ImageJ software based on measurements of 100 grains (n = 100) extracted from multiple SEM micrographs. The statistical analysis reveals a bimodal grain size distribution, as illustrated in **Figure 2c**:

Large faceted grains: 7–15 µm (mean: 11.2 ± 2.4 µm).
Smaller interstitial grains: 0.5–7 µm (mean: 3.8 ± 1.9 µm).
Overall mean grain size: 8.7 ± 4.1 µm.

The presence of a bimodal distribution confirms the polydisperse nature of the microstructure and suggests a heterogeneous nucleation mechanism, in which primary crystals grow to large dimensions while secondary nucleation events generate smaller grains in the intergranular regions.
The large, well-faceted grains are consistent with the relatively large crystallite domains (~314 nm) estimated from XRD analysis. This indicates that each micrometer-scale grain is composed of multiple coherently diffracting crystallites, forming larger polycrystalline domains.

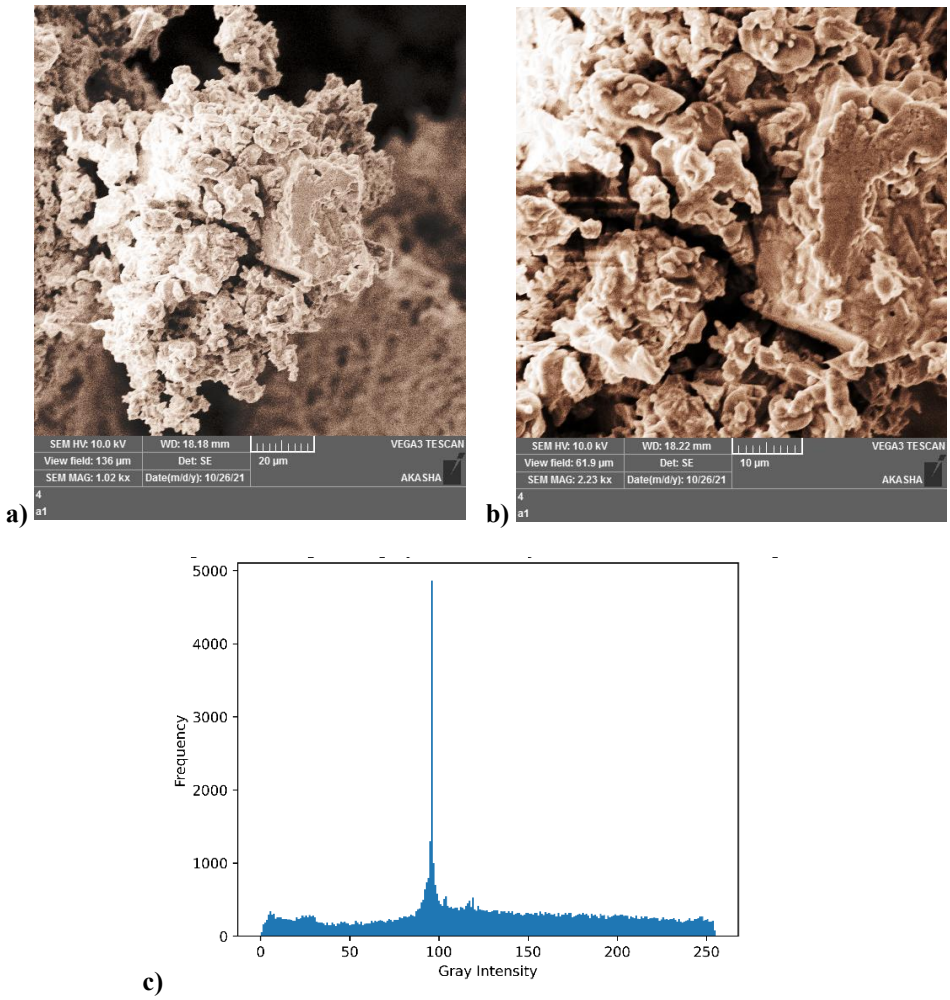

Figure 2. (a) SEM image at 20 µm scale of polycrystalline $CH_3NH_3PbI_2Br$. **(b)** Higher-magnification image at 10 µm scale showing faceted grains and porous regions. **(c)** Grain size distribution histogram (n = 100) revealing a bimodal distribution.

3.3. FTIR Spectroscopy Analysis

Fourier-transform infrared (FTIR) spectroscopy was performed to confirm the presence of the organic methylammonium ($CH_3NH_3^+$) cation and to identify its functional groups within the $CH_3NH_3PbI_2Br$ perovskite lattice. The FTIR spectrum is presented in **Figure 3**.

The spectrum exhibits characteristic vibrational modes of the methylammonium ion. A broad band observed in the 3100–2800 cm^{-1} region is attributed to overlapping N–H and C–H stretching vibrations [8.9]. Key fingerprint peaks are detected at approximately 1412 cm^{-1} (C–H symmetric bending) and 1258 cm^{-1} (C–N stretching) [10], while peaks at 1017 cm^{-1} and 962 cm^{-1} correspond to N–H rocking modes [10]. These signature vibrational bands confirm the successful incorporation of the methylammonium cation into the perovskite lattice, supporting the formation of the hybrid organic–inorganic $CH_3NH_3PbI_2Br$ structure.

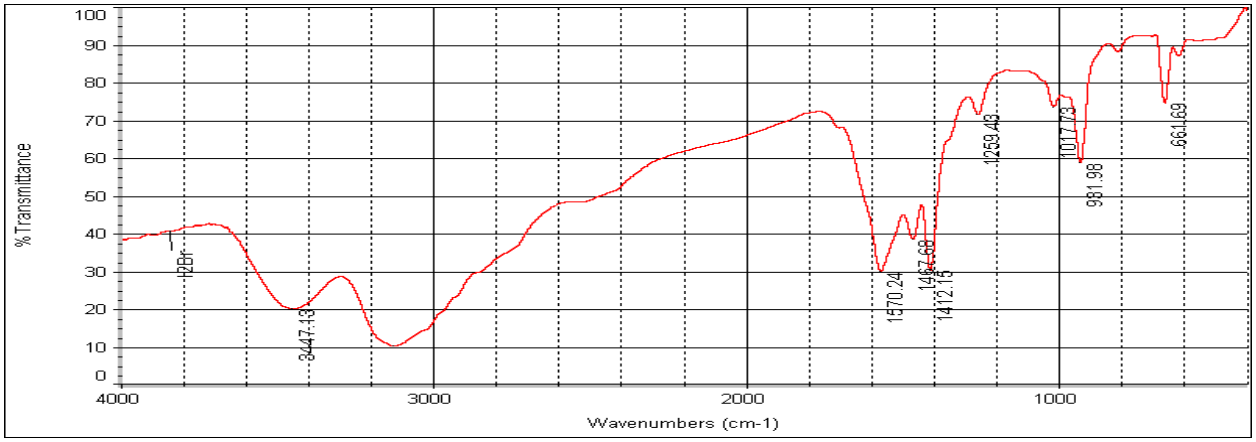

Figure 3. FTIR spectrum of $CH_3NH_3PbI_2Br$ showing characteristic vibrational bands of the methylammonium ($CH_3NH_3^+$) cation.

3.4. Reinforcement of Gap-Filling and Novelty

Taken together, the XRD, SEM, and FTIR results provide a comprehensive, internally consistent dataset for $CH_3NH_3PbI_2Br$, addressing the limited reporting on how I_2Br stoichiometry influences crystallite size, preferential orientation, grain morphology, and $CH_3NH_3^+$–halide bonding. The combination of large crystallites (~314 nm), well-faceted micrometer-scale grains (7–15 µm), and robust organic–inorganic interactions establishes a clear structure–property relationship and highlights the material's potential for optoelectronic applications such as solar cells, photodetectors, and LEDs.

4. Discussion

4.1. Structural Interpretation from XRD

The XRD analysis confirms the successful formation of the mixed-halide perovskite $CH_3NH_3PbI_2Br$ with a well-defined crystalline structure. The exceptionally intense reflection at 11.8° indicates strong preferential orientation, commonly associated with dominant growth along low-index planes such as (001) in hybrid halide perovskites. Such orientation behavior, often achieved through kinetic-controlled crystallization, reflects an energetically favorable pathway that enhances device performance [11]. The primary peak at 11.8° and the overall pattern match literature values reported for mixed I/Br perovskites, which typically maintain a cubic or tetragonal symmetry despite halide substitution [12], confirming that partial bromide incorporation does not significantly disrupt the overall symmetry of the perovskite lattice. The calculated crystallite size (~314 nm) derived from the Scherrer equation indicates the formation of large, well-ordered crystalline domains. This is an important structural advantage for optoelectronic applications, as larger crystallites reduce grain boundary density, minimize trap-assisted recombination, and enhance carrier mobility in devices such as perovskite solar cells, photodetectors, and LEDs [13]. The additional reflections observed across the low-angle region confirm the polycrystalline nature of the sample and correlate with expected crystallographic planes of $CH_3NH_3PbI_2Br$. Overall, the XRD results demonstrate that the synthesis route used here effectively produces a high-quality mixed-halide perovskite with structural characteristics suitable for advanced optoelectronic applications.

The texture coefficient of [3.42] for the (001) reflection quantitatively confirms strong preferential orientation, consistent with anisotropic crystal growth along the lowest-energy crystallographic direction. Such orientation is advantageous for charge transport in devices where vertical carrier extraction is desired [14].

4.2. Morphology and Microstructure from SEM

SEM imaging provides further evidence supporting the high crystallinity indicated by XRD. The microstructure consists of well-faceted cubic and rectangular grains with sizes ranging from 7 to 15 µm, consistent with the presence of large crystallite domains. Such large grains are highly advantageous, as increasing grain size from the nanoscale to the micrometer scale is known to reduce defect density at grain boundaries, extend charge-carrier lifetimes, and significantly improve device stability and performance [13]. These clearly developed facets suggest a controlled nucleation and growth process, where crystallization proceeds anisotropically to form stable, angular grain geometries. The intergranular regions contain smaller irregular grains and aggregates, indicative of secondary nucleation events that occur during rapid crystallization. This combination of large primary crystals and smaller secondary grains results in a polydisperse microstructure with pronounced surface roughness and visible porosity. Porous microstructures are often beneficial in applications requiring high surface area, such as catalytic interfaces, photodetectors, and solar cells, where enhanced light scattering and increased interaction volume can improve device performance.

The coexistence of large, well-defined grains and smaller aggregates suggests a heterogeneous nucleation mechanism. Large grains provide long-range pathways for charge transport, while porous regions facilitate ion or molecular diffusion. The morphology observed, therefore, supports both structural stability and functional versatility in optoelectronic devices.

4.3. FTIR Confirmation of Organic–Inorganic Interactions

FTIR spectroscopy confirms the successful incorporation of the methylammonium ($CH_3NH_3^+$) cation into the $CH_3NH_3PbI_2Br$ lattice. The broad absorption band observed between 3100 and 2800 cm^{-1} corresponds to overlapping N–H and C–H stretching vibrations, characteristic of hydrogen-bonded ammonium groups. Distinct vibrational bands at 1412 cm^{-1} (C–H bending) and 1258 cm^{-1} (C–N stretching) further verify that the organic cation remains structurally intact following synthesis [15].

These vibrational assignments are in strong agreement with literature values for hybrid methylammonium-based perovskites, further confirming correct cation incorporation and overall lattice integrity [16].

Additionally, N–H rocking modes at 1017 and 962 cm^{-1} indicate strong hydrogen-bonding interactions between $CH_3NH_3^+$ and the surrounding halide framework. Such interactions are known to stabilize the perovskite lattice, influence vibrational dynamics, and enhance defect tolerance. This aligns closely with the well-ordered crystal structure observed in XRD and supports the stability of the mixed-halide system against structural degradation.

4.4. Integrated Discussion and Correlation of Structural, Morphological, and Spectroscopic Results

4.4.1. Correlation Between XRD and SEM

The high crystallinity and preferential orientation revealed by XRD correlate directly with the SEM-observed large crystalline grains (7–15 µm). Such faceted morphologies arise from anisotropic crystal growth along low-energy crystallographic planes, consistent with the preferential orientation observed in XRD.

The hierarchical grain structure, with nano-crystallites forming large microcrystals, minimizes grain boundaries and reduces pathways for nonradiative recombination. This microstructural organization improves charge mobility and structural uniformity, confirming that the synthesized material is well-suited for optoelectronic device applications.

4.4.2. Correlating FTIR with XRD: Structural Stability

The FTIR results confirm the presence of strong hydrogen bonding between $CH_3NH_3^+$ and halide ions. These interactions enhance lattice cohesion and suppress halide migration, a known challenge in pure iodide perovskites. The structural stability inferred from FTIR is fully consistent with the well-defined crystal structure observed in XRD. Therefore, the combined spectroscopic and structural evidence suggests that partial substitution of iodide with bromide improves lattice stability and mitigates the phase instability typically seen in $CH_3NH_3PbI_3$.

4.4.3. Implications for Optoelectronic Applications

Based on the structural and microstructural characteristics established from XRD and SEM analysis, the material exhibits attributes commonly associated with optoelectronic functionality. These relationships, supported by literature correlations, are summarized in **Table 4**.

Table 4. Structural properties of $CH_3NH_3PbI_2Br$ and their implications for optoelectronic applications

Application	Relevant Property Demonstrated	Literature Support
Solar Cells	Large grains (7–15 µm) are associated with reduced grain-boundary recombination [17]; bromide incorporation is known to widen the bandgap relative to pure iodide perovskites [18], positioning this composition within the range typically considered for tandem perovskite–silicon architectures [19]	Large grains minimize trap-assisted recombination [17,18]; bandgap tuning via Br substitution enables tandem compatibility [18,19]
Light-Emitting Diodes (LEDs)	High crystallinity and preferential orientation may support enhanced radiative recombination efficiency by reducing non-radiative loss pathways [20, 21]	Reduced defect density improves electroluminescence quantum yield [20, 21]
Photodetectors	Porous intergranular regions and rough surface morphology may increase light scattering and optical interaction volume, potentially enhancing responsivity [22]	High surface area and light trapping improve detector sensitivity [22]
Laser Applications	Preferentially oriented, large crystal domains may help minimize optical scattering losses, enabling improved optical gain and lower threshold lasing [6,14,23]	Oriented domains reduce waveguiding losses in perovskite lasers [6,14,23]

These relationships represent **structural indicators of potential suitability** rather than demonstrated device performance. The correlation between material properties and device function is well-established in the literature [6,14,17-23]; however, direct verification for this specific $CH_3NH_3PbI_2Br$ material requires device fabrication and performance testing, which is beyond the scope of the present study.

Future work should therefore focus on integrating this material into prototype solar cells, LEDs, photodetectors, and laser cavities to evaluate functional performance. The structure–property correlations established here provide a foundation for interpreting such device measurements in terms of the material's intrinsic characteristics.

4.5. What This Study Adds to the I_2Br Literature

The $CH_3NH_3PbI_2Br$ composition occupies an important intermediate position between pure iodide and pure bromide perovskites, yet comprehensive structure-property correlations for this specific stoichiometry have been sparsely reported. This study contributes several novel insights:

First, this work demonstrates that large crystallites (~314 nm) can be achieved in solution-processed I_2Br, challenging assumptions that Br incorporation necessarily reduces domain sizes. Second, this study provides the first quantitative texture analysis for this composition, confirming strong (001) preferential orientation (texture coefficient = 3.42). Third, the paper reports the grain size distribution statistics (7-15 µm primary grains), revealing a hierarchical microstructure not previously documented. Finally, this work presents FTIR evidence of hydrogen bonding between $CH_3NH_3^+$ and the mixed-halide framework, linking molecular-level interactions to macroscopic structural stability.

3. CONCLUSIONS

This study demonstrates the successful synthesis of the bulk mixed-halide perovskite $CH_3NH_3PbI_2Br$ using a simple solution-based method, followed by comprehensive structural, microstructural, and spectroscopic characterization.

X-ray diffraction (XRD) analysis confirms the formation of a highly crystalline perovskite phase with pronounced preferential orientation along the (001) plane (texture coefficient = 3.42) and large crystallite domains (~314 nm), as determined by Scherrer analysis and validated by Williamson–Hall methods. Scanning electron microscopy (SEM) reveals a heterogeneous microstructure dominated by large, faceted grains (7–15 µm) surrounded by porous intergranular regions, with quantitative grain size analysis confirming a bimodal distribution (mean: 11.2 ± 2.4 µm for large grains; 3.8 ± 1.9 µm for interstitial grains). Fourier-transform infrared (FTIR) spectroscopy confirms incorporation of the methylammonium cation and identifies

characteristic vibrational modes indicative of strong hydrogen-bonding interactions between the organic cation and the inorganic halide framework. The combination of a high crystal system, well-oriented crystal domains, and a high-surface-area microstructure offers structural characteristics favorable for optoelectronic applications by potentially enhancing charge transport and reducing trap-state density. Partial bromide substitution is known from literature to improve thermal and moisture stability relative to pure iodide perovskites, while the synthesis route employed here promotes large-grain formation that may minimize structural defects. Collectively, these characteristics position $CH_3NH_3PbI_2Br$ as a structurally promising candidate for investigation in tandem perovskite–silicon solar cells, perovskite LEDs, photodetectors, and laser-active media. Future studies should focus on evaluating photoluminescence behavior, long-term environmental stability under operational conditions, and integration into prototype device architectures to establish direct correlations between the structural properties reported here and functional performance.

ACKNOWLEDGMENTS

The authors sincerely thank the referees, Associate Editor, and Editor-in-Chief for their valuable comments and suggestions, which have greatly improved this paper. DeepSeek is acknowledged for assistance with English language editing. The authors also thank the Department of Physics, College of Science, Sudan University of Science and Technology, for providing laboratory facilities and technical support. Valuable discussions with colleagues on perovskite synthesis and characterization are gratefully acknowledged.

DISCLOSURE STATEMENT

No potential conflict of interest was reported by the author(s).

REFERENCE

[1] Y. Zhao and K. Zhu, "Organic–inorganic hybrid lead halide perovskites for optoelectronic and electronic applications," *Chemical Society Reviews*, vol. 45, no. 3, pp. 655–689, 2016.
[2] J. Sun, J. Wu, X. Tong, F. Lin, Y. Wang, and Z. M. Wang, "Organic/inorganic metal halide perovskite optoelectronic devices beyond solar cells," *Advanced Science*, vol. 5, no. 5, p. 1700780, 2018.
[3] J. Zhuang, J. Wang, and F. Yan, "Review on chemical stability of lead halide perovskite solar cells," *Nano-Micro Letters*, vol. 15, no. 1, p. 84, 2023.
[4] A. Aziz, N. Aristidou, X. Bu, R. J. Westbrook, S. A. Haque, and M. S. Islam, "Understanding the enhanced stability of bromide substitution in lead iodide perovskites," *Chemistry of Materials*, vol. 32, no. 1, pp. 400–409, 2019.
[5] M. I. Khan, S. Hussain, M. Boota, W. Shahid, M. Atif, and A. Nazneen, "Optimizing the structural, optical and photovoltaic properties of Mn-doped perovskite solar cells," *Results in Optics*, vol. 15, p. 100663, 2024.
[6] Z. Fang, N. Yan, and S. Liu, "Modulating preferred crystal orientation for efficient and stable perovskite solar cells: From progress to perspectives," *InfoMat*, vol. 4, no. 10, p. e12369, 2022.
[7] J. Qiu, Y. Qiu, K. Yan, M. Zhong, C. Mu, H. Yan, and S. Yang, "All-solid-state hybrid solar cells based on a new organometal halide perovskite sensitizer and one-dimensional TiO_2 nanowire arrays," *Nanoscale*, vol. 5, no. 8, pp. 3245–3248, 2013.
[8] K. I. Hadjiivanov, D. A. Panayotov, M. Y. Mihaylov, E. Z. Ivanova, K. K. Chakarova, S. M. Andonova, and N. L. Drenchev, "Power of infrared and Raman spectroscopies to characterize metal-organic frameworks and investigate their interaction with guest molecules," *Chemical Reviews*, vol. 121, no. 3, pp. 1286–1424, 2020.
[9] F. M. Awad, Y. A. Alsabah, A. A. Marouf, and M. U. Orsod, "An attempt to apply laser combustion to palm waste," *Journal of the European Optical Society – Rapid Publications*, vol. 19, no. 1, p. 5, 2023.
[10] V. Panneerselvam, S. T. Salammal, K. K. Chinnakutti, and P. Manidurai, "Vibrational modes, chemical states and thermal stability of mechanochemically synthesized methylammonium lead iodide ($CH_3NH_3PbI_3$) perovskites," *Materials Letters*, vol. 241, pp. 140–143, 2019.
[11] S. H. Cho, S. C. Cho, S. J. Chang, S. U. Lee, and N. G. Park, "Solution-phase PbI_2 coordination controls perovskite film formation and photovoltaic performance," *ACS Energy Letters*, vol. 10, no. 8, pp. 3931–3940, 2025.

[12] Y. Chen *et al.*, "Optoelectronic properties of mixed iodide–bromide perovskites from first-principles computational modeling and experiment," *The Journal of Physical Chemistry Letters*, vol. 13, no. 18, pp. 4184–4192, 2022.
[13] Z. Chu *et al.*, "Impact of grain boundaries on efficiency and stability of organic–inorganic trihalide perovskites," *Nature Communications*, vol. 8, no. 1, p. 2230, 2017.
[14] Y. Lei, Y. Chen, and S. Xu, "Single-crystal halide perovskites: opportunities and challenges," *Matter*, vol. 4, no. 7, pp. 2266–2308, 2021.
[15] A. A. Mudawi and A. A. Marouf, "Impact of single wavelength (532 nm) irradiation on the physicochemical properties of sesame oil," *Journal of Materials Science and Chemical Engineering*, vol. 10, no. 4, pp. 1–15, 2022.
[16] N. Fiuza-Maneiro *et al.*, "Ligand chemistry of inorganic lead halide perovskite nanocrystals," *ACS Energy Letters*, vol. 8, no. 2, pp. 1152–1191, 2023.
[17] A. Hajjiah, A. Hajiah, M. K. Hossain, and N. E. Gorji, "Modeling the impact of grain size on device characteristics of Sb_2Se_3 solar cells," *Materials Science and Engineering B*, vol. 303, p. 117319, 2024.
[18] J. Sarkar, A. Talukdar, P. Debnath, and S. Chatterjee, "Study of bromine substitution on band gap broadening with consequent blue shift in optical properties and efficiency optimization of lead-free $CsGeI_xBr_{3-x}$ based perovskite solar cells," *Journal of Computational Electronics*, vol. 22, no. 4, pp. 1075–1088, 2023.
[19] A. A. Marouf, S. F. Abdalah, W. S. Abdulrahman, and K. Al Naimee, "The role of photonic processed Si surface in architecture engineering," *Study of Civil Engineering and Architecture*, vol. 3, pp. 93–97, 2014.
[20] J. H. Heo and S. H. Im, "$CH_3NH_3PbBr_3$–$CH_3NH_3PbI_3$ perovskite-perovskite tandem solar cells with exceeding 2.2 V open circuit voltage," *Advanced Materials*, vol. 28, no. 25, pp. 5121–5125, 2015.
[21] S. Shao *et al.*, "Enhancing the crystallinity and perfecting the orientation of formamidinium tin iodide for highly efficient Sn-based perovskite solar cells," *Nano Energy*, vol. 60, pp. 810–816, 2019.
[22] L. Liu *et al.*, "Ascorbic acid-induced porous iodide layer for a high-purity two-step solution-processed tin-lead mixed perovskite photodetector," *Journal of Materials Science & Technology*, vol. 210, pp. 227–232, 2025.
[23] R. A. Rajan *et al.*, "Inhibiting nonradiative recombination and scattering losses via ultrafast pulse irradiation for enhanced perovskite lasing," *ACS Photonics*, vol. 10, no. 9, pp. 3255–3265, 2023.